Editorial Board

The cover illustration shows views of a knee obtained after trauma in which the conventional x-ray images show only minimal abnormality of the bone while the MRI shows more extensive injury to the bone and ligaments. See Chapter 12, p. 671, Effects of Anatomical Structure on Signal Detection, Ehsan Samei, William Eyler and Lisa Baron.

HANDBOOK OF

Medical Imaging

Volume 1. Physics and Psychophysics

Jacob Beutel
Harold L. Kundel
Richard L. Van Metter
Editors

SPIE PRESS
A Publication of SPIE—The International Society for Optical Engineering
Bellingham, Washington USA

Samei E, Flynn MJ, Beute GH, Peterson E. "Comparison of Observer Performance for Real and Simulated Nodules in Chest Radiography." Proc SPIE 2712, 1996, pp. 60–70.

Samei E, Flynn MJ, Eyler WR, Peterson E. "The Effect of Local Background Anatomical Patterns on the Detection of Subtle Lung Nodules in Chest Radiographs." Proc SPIE 3340, 1998, pp. 44–54.

Samei E, Flynn MJ, Eyler WR. "Relative Influence of Quantum and Anatomical Noise on the Detection of Subtle Lung Nodules in Chest Radiographs." Radiology 1999 (accepted, in print).

Seeley GW, Roehrig H, Hillman BJ. "A Computerized Method for Measurement of Conspicuity: Comparison of Film and Digital Nephrograms." Invest Radio 19: 583–586, 1984.

Sharp PF, Philips R. "Physiological Optics." In Hendee WR, Wells PNT (Eds.) *The Perception of Visual Information*. New York, NY: Springer-Verlag, 1997.

Smith MJ. *Error and Variations Diagnostic Radiology*. Springfield, IL: Charles C. Thomas, 1967.

Stewart BK, Huang HK. "Single-Exposure Dual-Energy Computed Radiography." Medical Physics 17:866–875, 1990.

Vuylsteke P, Schoeters E. "Multiscale Image Contrast Manipulation (MUSICA)." Proc SPIE 2167, 1994, pp. 551–560.

Wallis RE, Walsh MT, Lee JR. "A Review of False Negative Mammography in a Symptomatic Population." Clin Radiol 44:13–15, 1991.

Waring JJ, Wasson WW. "The Imperfections of the Stereoscopic Maneuver in Radiography of the Chest." Radiology 6:298–203, 1926.

Whiting SW, Eckstein MP, Morioka CA, Eigler NL. "Effect of Additive Noise, Signal Contrast and Feature Motion on Visual Detection Structured Noise." Proc SPIE 2712, 1996, pp. 26–38.

Yao J, Barrett HH. "Predicting Human Performance by a Channelized Hotelling Observer Model." Proc SPIE 1768, 1992, pp. 161–168.

Zwicker RD, Atari NA. "Transverse Tomosynthesis on a Digital Simulator." Med Phys 24:867–971, 1997.

CHAPTER 13
Synthesizing Anatomical Images for Image Understanding

Jannick P. Rolland
School of Optics/CREOL, the University of Florida

CONTENTS

13.1 Introduction

The main goals of research in medical and biomedical imaging are to create "better" imaging systems, more accurate reconstructions, and develop methods of image processing that utilize the most important information present in an image or set of images, for accurate, timely, and cost-effective diagnosis and treatment of disease. How well desired information can be extracted best serves to define image quality and consequently the performance of imaging systems. Furthermore, as we deepen our understanding of medical images, new systems and new methods of image processing and image display may help optimize performance and assist radiologists in their challenge for accurate diagnostics.

Image quality is thus best measured by the performance of an observer on specific tasks [1]. The observer may be human such as a physician making a diagnosis, or a mathematical model such as an ideal observer [2], or a computer algorithm. Specific tasks may be the detection of a lesion in a chest x ray [3], the estimation of the percent stenosis of a detected aneurysm [4], or the registration of images such as the superimposition of anatomical atlases on patient data [5]. Regardless of the task considered, however, methods to assess image quality based on task performance are most important.

Traditionally, the conception of improved imaging systems in medical imaging has been accomplished by designing and constructing proposed systems and characterizing them from an engineering point of view, by reporting parameters such as resolution, modulation transfer function, and pixel signal-to-noise ratio. Naturally, such evaluation is not sufficient to predict the performance that the system will have in the clinic, given that it does not take into account either information about the types of objects being imaged or the tasks being carried out.

To fully assess the system, clinical trials based on specific tasks must be conducted. While clinical trials are required for final system assessment, the reliance on clinical trials for system design and optimization has severe limitations. First, the construction of proposed systems is costly and time consuming. In addition, if the system requires further optimization, it may take multiple trials and errors to find the best set of parameters and tradeoff to satisfy required task-based image-quality criteria. Finally, it is nearly impossible to know the anatomical underlying structures of the acquired clinical images unless the diagnosis is verified by physical examination. Instead, disease states are most often estimated by interpreting the images and looking for correlation with previous cases established statistically as well. The approach of building systems and conducting trial-and-error changes based on clinical images thus constitutes a highly impractical means of optimizing imaging systems.

For quantitative image-quality assessment, ensembles of images with equivalent statistics are required. When anatomical structures are imaged, it is important to note that the statistical properties are not only unknown, but are widely varying from patient to patient. It can therefore be elusive in several cases to attempt to classify clinical images in order to form statistical ensembles for image-quality assessment. For example, breast tissues vary on a quasi-continuum in terms of

fibrosity and fat amount, and establishing classes of images with equivalent statistical properties is not always possible with clinical images.

Another approach to improving imaging systems in medical imaging is to employ images acquired from mechanical phantoms. While mechanical phantoms are well specified, the main limitation is typically the lack in flexibility to vary parameters in the phantom to account for either natural variations in the data, or the presence of different types of abnormality.

In this chapter, we shall describe how synthetic images of anatomical images obtained either from a mathematical or a procedural model provide a useful tool to enhance our understanding of images. We shall also discuss how they enable quantifying image quality without the limitations of other methods previously mentioned. Employing synthetic images also has the benefit to yield cost-effective investigations.

In order to ensure a realistic level of complexity, synthetic images that model the statistics of anatomical images are desired to ensure transfer of findings to image-quality assessment of clinical images. If we cannot demonstrate the validity of a predictive task-based model in mathematically specified images relevant to medical imaging, we foresee that such a model will most likely fail to predict performance in clinical images.

In this chapter, we provide methods for synthesizing several types of synthetic images: angiograms, lumpy backgrounds, nuclear-medicine liver scans, ultrasound B scans, and generally speaking textured images with application to simulation of x-ray mammograms. The statistical properties of statistically defined images or image components are detailed.

13.2 Computer-simulated angiograms

Angiography is a radiological imaging modality that allows visualization of the normally radioluscent vascular anatomy. High radiographic attenuation is achieved in the vessels of interest by the injection, prior to exposure with diagnostic radiation, of a radio dense contrast agent. One of the many tasks performed with this modality is to detect or measure the extent of aneurysms or stenoses in blood vessels. The presence of such blood-vessel abnormality may be indicative of vascular disease, and accurate diagnosis is essential in prevention of catastrophic vascular malfunction resulting from the rupture of an aneurysm or constricted blood flow in a major vessel.

The motivation for employing computer-simulated angiograms comes from the need to precisely control the stimuli in performance experiments employing either the human observer or a mathematical observer. We shall show that aspects of the vessel generation in three dimensions can be parameterized in order to enable acquisition of tightly specified, but realistic stimuli. Moreover, statistically defined curvature and torsion, as well as irregular edges further allow for realistic, yet mathematically specified, blood vessels.

Tasks that have been considered using these simulated images are the detection and the estimation of aneurysms and stenoses for image understanding and

medical-image interpretation. Specifically, computer-generated angiograms were employed in testing by means of psychophyscial experiments whether the curvature of the blood vessel at the location of a lesion had any impact on the detectability of the lesion in both a location known exactly and in a search task.

In a location known-exactly task, the detectability of lesions was measured. We found that the detection thresholds increased with curvature [6]. This experiment was then followed by an investigation of lesion detectability in a search experiment, referred to as lesion saliency. The more salient a lesion, the faster it was found. In this location-unknown task, the percent narrowing or bulging of the blood vessel was adjusted for all lesions to be equally detectable in a location known-exactly task. We then found that curvature had no impact on the saliency of the lesions. They were all equally salient once equally detectable in a location known-exactly task [7]. This experiment led to deeper understanding of lesion detection in angiograms, and allowed us to investigate independently detectability in a location known-exactly task versus detectability in a search task, where location was unknown.

The computer-generated angiograms were also used in some estimation task experiments. Under controlled conditions, the ability of human observers to estimate a change in the shape of a blood vessel corresponding to either some aneurysm or a stenosis embedded in a tree of similar shaped objects (i.e., blood vessels) was measured. In these experiments, the control of the stimuli allowed to investigate the accuracy of estimation as a function of the location of the lesion with respect to other underlying structures close to the blood vessels [8].

Another task that may be considered with computer-simulated angiograms is the assessment of 3D reconstruction algorithms. In this case, branching blood vessel trees would be required. An algorithm for simulating individual three-dimensional (3D) blood vessels with lesions in user-specified regions of interest is now described. The methods may be extended to simulation of branching blood vessel trees.

13.2.1 Overall approach for angiogram simulations

The simplest simulation of an angiogram with realistic geometry of individual blood vessels may be achieved by simulating individual three-dimensional blood vessels that curve and twist in a predefined volume, followed by the summation of several of their projections [9]. While clinical angiograms clearly possess many branching blood vessels, the simple approach to angiogram simulation described here leads to images that have been mistaken to be real angiograms by radiologists. Moreover, the simulation of 3D individual blood vessels described here constitutes the foundation for developing a method for branching blood vessels.

The approach to blood vessels simulation consists in viewing 3D blood vessels as general cylinders defined by a medial axis, and a corresponding diameter function coupled with a curvature and torsion associated with each point along the axis. The simulation of an individual blood vessel consists then of the following steps: (1) generating a space curve that bends and twists in space, which mathematically

represents the medial axis of the blood vessel, (2) defining a region of interest on the two-dimensional (2D) projection of the space curve to locate potential lesions, (3) generating the 3D blood vessel from a space curve and the parameters that characterize the blood vessel; for example, diameter, type of lesion if any, lesion parameters such as the size of the lesion, and (4) generating one or several 2D projections of the 3D blood vessel. Each step of the simulation is now described.

13.2.2 Space curve generation

Initially, a curve is generated which specifies the path of the vessel in three-dimensional space as shown in Figure 13.1. The curve is specified by the Frenet formulas that mathematically specify the curvature and the torsion of a space curve as the curve traces a path in space. The Frenet description given by O'Neill Barrett (1966) can be summarized as follows [10].

The velocity vector of a curve β at position s is $\beta'(s)$, and the speed of the curve at s is the length of the velocity vector, or $\|\beta'(s)\|$, where the double-side bar denotes the norm of a vector. Let β be a unit speed curve, such that along β, $\|\beta'(s)\| = 1$. Then $\mathrm{T} = \beta'$ is called the unit *tangent vector* field on β. The derivative of T denoted T′ equal β'' and measures the way in which the curve is turning in space. T′ is called the *curvature vector* field of β. The length of T′ gives a numerical measurement of the turning of β. The function $\kappa(s)$ equal $\|\mathrm{T}'(s)\|$ is called the *curvature function* of β. κ is positive and the larger κ, the sharper is the turning of β. T′ is always normal to β. If we impose the restriction that κ is strictly positive, then the unit vector field N equal T'/κ on β indicates the *direction* in which β is turning at each point, and is called the *principal normal vector* field of β. Then the vector field B equal T cross product N on β is called the *binormal vector* field of β.

The three vector fields T, N, and B are unit vectors that are mutually orthogonal at each point along the curve. The set of these three vectors (T, N, B) is called the Frenet frame field of β. The key to the successful study of the geometry of a curve β is to use its Frenet frame field, for it contains all descriptive information about β.

The Frenet formulas then express the change or derivatives (T′, N′, B′) of the Frenet frame field (T, N, B). If β is a unit-speed curve with curvature κ (s) and torsion $\tau(s)$ then

$$\begin{aligned} \mathrm{T}' &= \kappa \mathrm{N}, \\ \mathrm{N}' &= -\kappa \mathrm{T} + \tau \mathrm{B}, \\ \mathrm{B}' &= -\tau \mathrm{N}. \end{aligned} \tag{13.1}$$

Given the curvature and torsion functions along the curve or values at each point along the arc length of the space curve, the Frenet formulas can be used to compute the new Frenet frame field at a point $s + \delta s$ as a function of κ, τ, and (T, N, B) at s. In the simulation, a curvature κ and torsion τ are chosen at each point along the space curve according to specified statistical distributions about previous values as we shall describe. The next location in space (x, y, z) of the

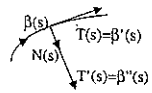

Figure 13.1: Definition of the normal and tangent to a space curve.

space curve is then computed given a small increment in arclength δs and the coordinates T_x, T_y, and T_z of the tangent vector along x, y, and z at s.

13.2.3 Curvature and torsion specification

The values of curvature and torsion along the space curve are defined statistically to allow for realistic simulations. Because 3D angiograms are not readily or even typically available, and realistic simulations may only be obtained if the blood vessels are first simulated in 3D before being projected, we have selected a range of variation based on theoretical ground (i.e., positivity constraint) as well as empirical investigations.

The curvature may be specified to take on values greater than 0 and less than or equal to 0.3. These values correspond to an infinite radius of curvature (i.e., a straight curve) and a radius of curvature equal to about 3 pixels, respectively. Smaller radii of curvature were disallowed.

Following the requirement that the curvature κ be positive, a Poisson distribution for small values of the curvature or an approximation to a Poisson distribution for larger values is a natural choice. Another possible choice would be a Gaussian with positivity constraint. A Poisson distribution was chosen in the simulation demonstrated, and the values of κ were thus first scaled by a factor of 1000 in order to work with integer values.

For such a range, if the scaled previous curvature value is less than 10 or greater than 290, the next value is chosen according to a Poisson distribution about the scaled previous value. If the previous curvature value is within those two values, the next value is chosen from a Gaussian distribution whose mean value equals the scaled previous curvature value, and whose standard deviation equals the mean.

In the same way that curvature values greater than 0.3 were disallowed, torsion values τ were restricted to the range -0.3 to 0.3. New values of τ are sampled from a Gaussian distribution of standard deviation small with respect to the range to ensure a smooth change in torsion as the curve is generated. A Gaussian, whose mean value was the previous torsion value, and the standard deviation was 0.02, was chosen.

Finally, if the newly selected curvature or torsion values were outside their range of variation (0.0 to 0.3 for κ, and -0.3 to 0.3 for τ), or the percent change in the curvature or torsion was greater than 30%, the current curvature or torsion was assigned to the previous value. A mechanism for preventing extensive or continuous high curvature or torsion "loops" that would lead to "pig tails" was also put into place. A count of consecutive curvature and torsion values greater than 0.29

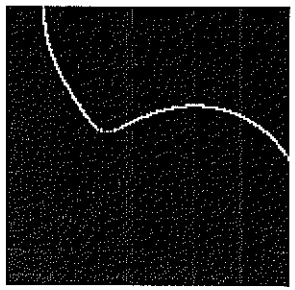

Figure 13.2: An example of a 2D projected space curve.

was kept. When the count exceeded a value as a function of δs, a new curvature or torsion value was assigned, which was in the case presented here the previous curvature or torsion divided by a factor of three.

From the space curve, a projected space curve denoted $\kappa_{2D}(s)$ is generated as shown in Figure 13.2. A file however maintains values of s, κ, and τ for each position along the curve, as well as the 2D curvature values of the projected space curve (O'Neill, 1966) [10]. The validation of the range of values selected for the curvature and the torsion of the 3D blood vessels, while not conducted in the work referenced here, would consist in comparing the values of $\kappa_{2D}(s)$ obtained in the simulated blood vessels to that of clinical 2D angiograms.

13.2.4 Blood vessels and possible lesions simulation

The positions at which lesions (i.e., aneurysms or stenoses) may form in the vessel can be specified along the projected space curve, where user-defined regions of interest (ROIs) may be specified as shown in Figure 13.3. While specified along the projected, thus 2D, space curve, the ROIs location and dimensions subsequently serves in the generation of the 3D blood vessels.

Starting with the generation of a single blood-vessel angiogram, at each position along the space curve defining the location of the blood vessel, a solid sphere of specified diameter is placed. The simulation of the 3D blood vessel is equivalent to rolling the sphere along the 3D space curve. Possible lesions are then automatically generated in 3D by allowing the sphere to vary in diameter within the specified ROIs.

The shape of lesions may be specified by some function. We shall demonstrate the case of a Gaussian function of given height and width, where the height represents the percent fraction of the blood-vessel diameter, and the width represents the length of the lesion expressed in units of pixel. Specifically, the sum of a constant and a Gaussian function centered at the location of a lesion, for example, describes the diameter of the rolling sphere as it passes through the lesion region.

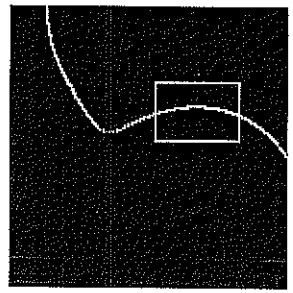

Figure 13.3: A region of interest has been drawn on the projected curve.

13.2.5 Example of simulated angiograms

To simulate 2D angiograms, 3D blood vessels, with or without lesions, are generated individually and projected in a 2D plane. An example of a segment of a blood vessel with an aneurysm is shown in Figure 13.4. Additional examples are shown in Figures 13.5 and 13.6. In Figure 13.5, the vessel has a diameter of 10 pixels, and a 50% aneurysm of length 20 pixels located in the lower right corner. In Figure 13.6, the vessel has an initial diameter of 15 pixels which tapers by a factor of -0.001 from its starting position, and a 50% stenosis of length 10 pixels positioned roughly halfway along the path of the vessel, near the center of the image. The images shown here were cropped from 256×256 images.

Individual 2D blood vessels can then be added. Examples are shown in Figure 13.7. In the case of the simulation shown, all blood vessels had the same diameter, except at the location of lesions, as required for a controlled psychophysical experiment where we did not want the diameter of the blood vessels to create a confounding factor for studying the effect of curvature on detection [7]. Simulations may include blood vessels of different, as well as spatially varying, diameter.

13.2.6 Simulation of edge noise

The diameter of the blood vessel may be varied randomly as well in order to simulate natural variations in the diameter of the vessel walls. In a healthy patient, vessel walls are indeed smooth. However, in older patients or patients with vascular disease such as artherosclerosis, small plaques form on the interior wall of the vessel, causing the vessel imaged with contrast agent to have a lumpy or non-smooth boundary. We shall refer to such variations as edge noise.

Edge noise can be generated by employing grayscale morphology methods to randomly erode or dilate the level contours in the image [9]. The lumpy appearance of the boundary of the vessel is a form of texture. The generation of noise is done iteratively. The number of iterations dictates, along with the correlation of

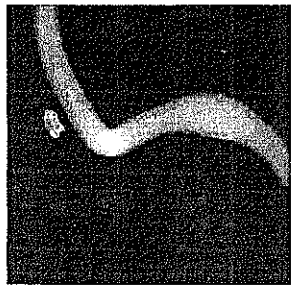

Figure 13.4: A blood vessel was generated with an aneurysm in the specified region of interest in 3D. The 2D projection is shown.

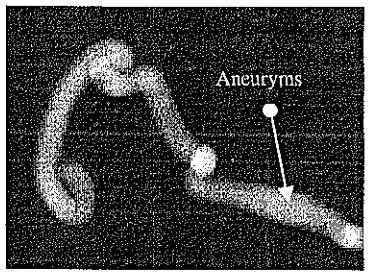

Figure 13.5: A blood vessel with an aneurysm is shown.

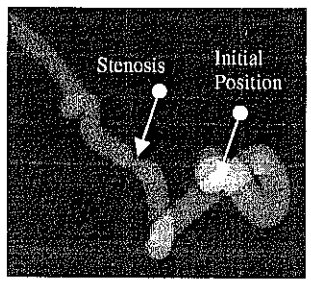

Figure 13.6: A blood vessel with an stenosis is shown.

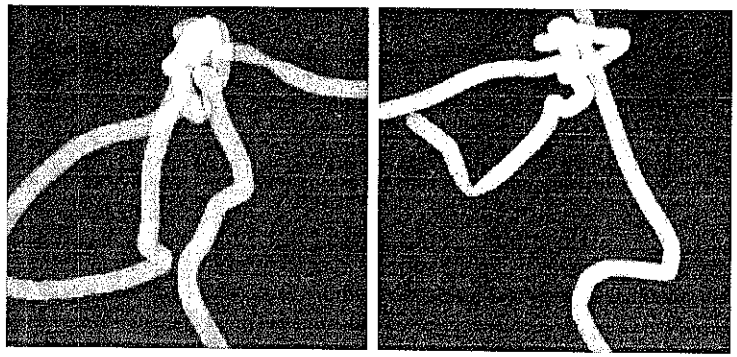

Figure 13.7: Examples of computer-simulated angiograms.

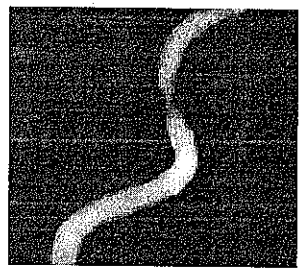

Figure 13.8: Edge noise was added to the blood-vessel simulation.

the noise, the extent of the effect. An example of edge noise simulation is shown in Figure 13.8.

13.2.7 Statistical ensembles

As stated in Section 13.1, quantitative image-quality assessment requires ensembles of images with equivalent statistics. The ability to mathematically synthesize blood vessels importantly allows us to define classes of images with equivalent statistical descriptions regarding the geometry of the blood vessels such as their distributions of curvature, torsion, and blood-vessel diameters, as well as the types of lesions and their locations. For example, in the studies reported by Rolland *et al.* (1996) [7], ensembles of computer-simulated angiograms with lesions at either low, medium, or high curvature values were generated to investigate the effect of curvature on lesion detection.

13.3 Synthesizing lumpy backgrounds

The need for spatially varying backgrounds was generated by an unsolved problem in planar emission imaging systems. Such a system generally consists of an x ray or gamma-ray source, an aperture element, and a detector. The challenge was how to specify the optimal photon-collecting aperture. Large apertures yield high photon counts but with positional uncertainty or poor resolution, while small apertures yield low photon counts and high resolution.

Finding the optimal trade-off between collection efficiency and resolution is important in the design and utilization of these systems, and requires quantitative specification of the imaging system from object space to the detector. The most challenging is typically the specification of the object to be imaged, which may be thought of as the combination of a lesion embedded in an anatomical background, or as an anatomical image that may or may not present abnormal changes in its texture. Examples of such objects are lesions and architectural distortions in mammographic images, respectively.

Cases of backgrounds where the performance of statistical observer models could be easily calculated were given in Chapter 9. The case of a known-exactly lesion (i.e., characteristics and location are exactly specified) embedded in an infinite uniform background of known strength led to an aperture which is infinite in extent. The generalization of this problem to include a background of unknown strength combined with a finite detector size led to the contrary to a finite optimal aperture size which better reflects clinical experience [11].

Another problem, presented by Wagner *et al.* (1981) consisted of a high-contrast Rayleigh task in which the ideal observer was computed to determine whether a noisy image was that of a single or double Gaussian two-dimensional signal [12]. Harris (1964) suggested that this discrimination task as a function of the object width and separation is a useful test of imaging system performance [13]. What was referred to as the signal in the Wagner paper, is the equivalent of a lesion in medical imaging. The signal was superimposed in this case on a uniform background of known and constant strength. The only randomness in the image resulted from Poisson statistics. Wagner *et al.* chose to image this object through different apertures including a pinhole and a large open aperture twenty times the size of the pinhole. They found that, for the ideal observer, the large aperture outperformed the small pinhole for all source widths and separations. This finding did not agree with experimental practices in emission imaging. For example, in nuclear medicine, spatial resolution of 1 cm, measured as the width of the point spread function, seems to give the best subjective image quality. The detection and Rayleigh tasks that found superior performance for large apertures have two common features: one is the complete specification of the background and signal, the other is the infinite size of the detector area.

To investigate the paradox brought by the Tsui and Wagner studies, Myers *et al.* (1990) increased the complexity of the task by relaxing the property of an exactly specified background while keeping the object size and similarly the detector size

infinite [14]. Specifically, researchers simulated spatially varying backgrounds that are known as lumpy backgrounds [15, 16]. Detectability of several mathematical observers was computed and it was found that the Hotelling observer predicted an optimal aperture size for detectability, also found for the human observer.

The intent behind the lumpy-backgrounds simulation was not to replicate mathematically specific types of images. Rather it was intended to simply allow for the spatially varying property often encountered in medical images, while ensuring that the gray-level statistical properties were fully determined and known so that the performance of mathematical observers could be computed and hypotheses tested. Lumpy backgrounds have since been employed in various image-quality assessment tasks for medical imaging [17–21]. It is implicitly assumed in such approaches to simulating quasi-anatomical images that a system optimized for a model observer and a specified task would also be optimal not only for the human observer but also for more realistic tasks.

13.3.1 Assumptions for the simulation of lumpy backgrounds

In the simulation of lumpy backgrounds, the ability to create a spatially inhomogeneous background while knowing its first and second-order statistical properties are of primary importance. The variability in the background can be achieved in many different ways, but only certain models lead to descriptions that are mathematically tractable [16].

We make several assumptions to simplify the mathematics. First, we assume that the background is a wide-sense stationary process, where the autocorrelation function is a function of only the distance $\mathbf{r}$ between two observation points. Second, we assume that the background autocorrelation function is a Gaussian function of the form

$$R_f(\mathbf{r}) = \frac{W_f(0)}{2\pi r_b^2} \exp\left(-|\mathbf{r}|^2/2r_b^2\right), \tag{13.2}$$

where r_b is the correlation length of the autocorrelation function and $W_f(0)$ is the value of the power spectrum at zero frequency. The subscript f here emphasizes the fact that the autocorrelation function refers to the object $f(\mathbf{r})$ rather than the image $g(\mathbf{r})$. The notation $W_f(0)$ comes from the notations used for the power spectrum because, for stationary statistics, the power spectrum $W_f(\boldsymbol{\Delta})$ can be defined as the Fourier transform of the autocorrelation function, so that

$$W_f(\boldsymbol{\Delta}) = W_f(0) \exp\left(-2\pi^2 r_b^2 |\boldsymbol{\Delta}|^2\right), \tag{13.3}$$

where $\boldsymbol{\Delta}$ is the 2D frequency variable in the Fourier domain conjugate to $\mathbf{r}$. $W_f(0)$ is chosen as a measure of lumpiness. We shall now proceed to a description of two simulation schemes that yield stationary statistics and Gaussian autocorrelation functions.

13.3.2 Type-I lumpy backgrounds

The first approach to lumpy backgrounds is to simulate uncertainty in the image by randomly superimposing Gaussian functions upon a constant background of strength B_0 over the object space [15]. We refer to these Gaussian functions as Gaussian blobs or simply blobs. To keep the mathematics simple, we assume that the Gaussian blobs are of constant amplitude $b_0/\pi r_b^2$ and constant half-width r_b. An object formed with these blobs can be described mathematically as the sum of two terms: a constant term and a lumpy component term. The lumpy component term is the convolution of a set of delta functions of equal amplitude randomly located in object space, with a Gaussian function of constant strength and width. The lumpy component of the background, denoted $b(\mathbf{r})$, is then given by

$$\begin{aligned} b(\mathbf{r}) &= \left[\sum_{j=1}^{K}\delta(\mathbf{r}-\mathbf{r}_j)\right] * \left[\frac{b_0}{\pi r_b^2}\exp\left(-\frac{|\mathbf{r}|^2}{r_b^2}\right)\right] \\ &= \sum_{j=1}^{K}\frac{b_0}{\pi r_b^2}\exp\left(-\frac{|\mathbf{r}-\mathbf{r}_j|^2}{r_b^2}\right), \end{aligned} \tag{13.4}$$

where $\mathbf{r}_j$ is a uniformly distributed random variable over the object area that describes the location of the jth blob, and K is the number of blobs in the background. Note that r_b is the $1/e$ width of the blobs as well as the correlation length (defined as a standard deviation) of R_f.

The description of a nonuniform background given by Eq. (13.4) is not sufficient to yield a Gaussian autocorrelation function. The calculation of the autocorrelation function presented in Section 13.3.3 shows that the number of blobs K must itself be a random variable with the mean of K equal to its variance. A Poisson distribution is chosen for K as it will satisfy this condition. The expression for $R_f(\mathbf{r})$ reduces to

$$R_f(\mathbf{r}) = \frac{\overline{K}}{A_f}\frac{b_0^2}{2\pi r_b^2}\exp\left(-\frac{|\mathbf{r}|^2}{2r_b^2}\right), \tag{13.5}$$

where A_f is the area of the object. The expression for R_f, or equivalently W_f given by

$$W_f(\boldsymbol{\Delta}) = \frac{\overline{K}}{A_f}b_0^2\exp\left(-2\pi^2 r_b^2|\boldsymbol{\Delta}|^2\right) \tag{13.6}$$

describes the complete second-order statistics of the lumpy background thus generated. By comparing Eq. (13.3) to Eq. (13.6), we find that the lumpiness, measured in units of counts^2/(s^2 mm^2) is given by

$$W_f(0) = \frac{\overline{K}}{A_f}b_0^2. \tag{13.7}$$

We note that lumpiness as defined is a function of only the mean number of blobs per unit area and the strength of the blobs, not their actual size and shape. The size and shape of the blobs may be an important factor, however, in relation to the task to be performed. For example, in a lesion-detection task, the shape and size of the blobs are important in relation to the size and shape of the lesion to be detected.

13.3.3 Computation of first and second-order statistics for type-I lumpy backgrounds

The random variable used to describe the lumpiness in the background given by Eq. (13.4) can be written as

$$b(\mathbf{r}) = \left[\sum_{j=1}^{K}\delta(\mathbf{r}-\mathbf{r}_j)\right] * y(\mathbf{r}), \tag{13.8}$$

where the asterisk denotes 2D convolution, and

$$y(\mathbf{r}) = \frac{b_0}{\pi r_b^2}\exp\left(-\frac{|\mathbf{r}|^2}{r_b^2}\right). \tag{13.9}$$

The first-order statistics can be expressed most generally as the gray-level histogram averaged over the ensemble of objects. In the case of lumpy backgrounds, the histogram is Gaussian by construction. The mean of the histogram, which is also the expected value $\overline{B}$ of the background over the ensemble of objects, can be derived analytically and its expression will be required in the computation of second-order statistics. The expression for the mean level $\overline{B}$ is given by

$$\begin{aligned} \overline{B} &= B_0 + \langle b(\mathbf{r})\rangle_{f,K} \\ &= B_0 + \left\langle \sum_{j=1}^{K}\frac{1}{A_f}\int \mathrm{d}^2\mathbf{r}_j\, y(\mathbf{r}-\mathbf{r}_j)\right\rangle_K \\ &= B_0 + \frac{\overline{K}}{A_f}b_0, \end{aligned} \tag{13.10}$$

where we assumed that A_f tends to infinity, and $\langle b(\mathbf{r})\rangle_{f,K}$ is the expectation value of $b(\mathbf{r})$ averaged over two random variables, the random positions r_j for a fixed number of blobs (i.e., average over f), and the various values of K. Note that B_0 is in units of counts/(s mm^2), $\overline{K}/A_f$ is in units of counts/mm^2, and b_0 is in units of counts/s. The mean background $\overline{B}$ is then expressed as the number of counts/(s mm^2).

For a Gaussian random process, the second-order statistics is fully described by the autocorrelation function. Similarly, to compute the autocorrelation of this

random process, we shall average over f and K. The autocorrelation of the lumpy background $b(\mathbf{r})$ is given by

$$\begin{aligned} R_f(\mathbf{r}) &= \langle R_{f|K}(\mathbf{r}' - \mathbf{r}'') \rangle_K \\ &= \langle \langle [b(\mathbf{r}') - \langle b(\mathbf{r}') \rangle_{f|K}] [b(\mathbf{r}'') - \langle b(\mathbf{r}'') \rangle_{f|K}] \rangle_{f|K} \rangle_K, \end{aligned} \tag{13.11}$$

where $\mathbf{r}''$ and $\mathbf{r}'$ are 2D position vectors and $\langle b(\mathbf{r}') \rangle_{f|K}$ is the expectation value of $b(\mathbf{r}')$ averaged over the random positions of blobs that constitute the lumpy backgrounds. The expression for $R_{f|K}$ given in Eq. (13.11) can be shown to reduce to the difference of two terms [16]

$$R_{f|K}(\mathbf{r}) = \langle b(\mathbf{r}') b(\mathbf{r}'') \rangle_{f|K} - \langle b(\mathbf{r}') \rangle_{f|K} \langle b(\mathbf{r}'') \rangle_{f|K}. \tag{13.12}$$

The second term of Eq. (13.12) is given by

$$\langle b(\mathbf{r}') \rangle_{f|K} \langle b(\mathbf{r}'') \rangle_{f|K} = \left\langle \sum_{j=1}^{K} y(\mathbf{r}' - \mathbf{r}_j) \right\rangle_{f|K} \left\langle \sum_{j=1}^{K} y(\mathbf{r}'' - \mathbf{r}_j) \right\rangle_{f|K} = K^2 \frac{b_0^2}{A_f^2}. \tag{13.13}$$

The first term of Eq. (13.12) can be written

$$\begin{aligned} \langle b(\mathbf{r}') b(\mathbf{r}'') \rangle_{f|K} &= \left\langle \sum_{i=1}^{K} y(\mathbf{r}' - \mathbf{r}_i) \sum_{j=1}^{K} y(\mathbf{r}'' - \mathbf{r}_j) \right\rangle_{f|K} \\ &= \int \mathrm{d}^2 r_1 \, \mathrm{pr}(\mathbf{r}_1) \ldots \int \mathrm{d}^2 r_K \, \mathrm{pr}(\mathbf{r}_K) \\ &\quad \times \sum_{i=1}^{K} y(\mathbf{r}' - \mathbf{r}_i) \sum_{j=1}^{K} y(\mathbf{r}'' - \mathbf{r}_j), \end{aligned} \tag{13.14}$$

where $\mathrm{pr}(\mathbf{r}_i)$ is the probability associated with the random variable $\mathbf{r}_i$. If $i = j$, each term of the sum over i and j contributes in the same fashion to term 1. Since there are K terms such that $i = j$, the first term of Eq. (13.12) becomes for $i = j$,

$$\langle b(\mathbf{r}') b(\mathbf{r}'') \rangle_{f|K} (i = j) = \frac{K}{A_f} \frac{b_0^2}{2\pi r_b^2} \exp\left(-\frac{|\mathbf{r}|^2}{2r_b^2} \right). \tag{13.15}$$

Similarly, since they are $(K^2 - K)$ terms with $i \neq j$, the contribution of the terms $i \neq j$ to the first term of Eq. (13.12) is given by

$$\langle b(\mathbf{r}') b(\mathbf{r}'') \rangle_{f|K} (i \neq j) = (K^2 - K) \frac{b_0^2}{A_f^2}. \tag{13.16}$$

Thus the autocorrelation function R_f is given by

$$R_f(\mathbf{r}) = \frac{\overline{K}}{A_f} \frac{b_0^2}{2\pi r_b^2} \exp\left(-\frac{|\mathbf{r}|^2}{2r_b^2} \right) + \left(\overline{K^2 - K} \right) \frac{b_0^2}{A_f^2} - \overline{K}^2 \frac{b_0^2}{A_f^2}, \tag{13.17}$$

which is Gaussian only if K satisfies $(\overline{K^2 - K}) = \overline{K}^2$ or $(\overline{K^2} - \overline{K}^2) = \overline{K}$. If K is a Poisson random variable, such relationship will be satisfied and the autocorrelation reduces to a Gaussian given by

$$R_f(\mathbf{r}) = \frac{\overline{K}}{A_f} \frac{b_0^2}{2\pi r_b^2} \exp\left(-\frac{|\mathbf{r}|^2}{2r_b^2} \right). \tag{13.18}$$

The power spectrum, which is defined as the Fourier transform of the autocorrelation function is given by

$$W_f(\boldsymbol{\Delta}) = \frac{\overline{K}}{A_f} b_0^2 \exp(-2\pi^2 r_b^2 |\boldsymbol{\Delta}|^2) \quad \text{thus} \quad W_f(0) = \frac{\overline{K}}{A_f} b_0^2. \tag{13.19}$$

13.3.4 Type-II lumpy backgrounds

A second approach to lumpy backgrounds with a Gaussian autocorrelation function is to filter uncorrelated Gaussian noise. If the filter function is chosen to be a Gaussian function of correlation length r_b, a mathematical description of the background generated from filtered uncorrelated Gaussian noise is best given in the discrete form

$$b(\mathbf{r}_j) = \sum_i a(\mathbf{r}_i) \frac{H(0)}{\pi r_b^2} \exp(-|\mathbf{r}_j - \mathbf{r}_i|^2 / r_b^2), \tag{13.20}$$

where $a(\mathbf{r}_i)$ is a random variable normally distributed with mean value A_0 and standard deviation σ, with i specifying the ith blob located at the ith pixel, and r_j is the location of the jth pixel in the background. In this model, the randomness resides in the amplitude of the Gaussian blobs instead of in their position.

13.3.5 Computation of first and second-order statistics for type-II lumpy backgrounds

The mean background $\overline{B}$ of the random process $b(\mathbf{r}_j)$ can be evaluated by taking the ensemble average over the random variable, which in this case, is the amplitude of the noise impulses at each pixel location j in the image. $\overline{B}$ is given in counts/(s pixel) by

$$\begin{aligned} \overline{B} &= \langle b(\mathbf{r}) \rangle_a \\ &= \left\langle \frac{H(0)}{\pi r_b^2} \sum_i a(\mathbf{r}_i) \exp(-|\mathbf{r}_j - \mathbf{r}_i|^2 / r_b^2) \right\rangle_a \\ &= \frac{1}{\varepsilon^2} H(0) A_0, \end{aligned} \tag{13.21}$$

where A_0 in units of counts/(s pixel) is defined as $\langle a(\mathbf{r}_i)\rangle_a$, and ε^2 is the pixel area.

By definition, the power spectrum of uncorrelated noise $W(\boldsymbol{\Delta})$ is constant, and if we denote by $H(\Delta)$ the Gaussian filter used to filter Gaussian noise, the resulting power spectrum is given by

$$W_f(\boldsymbol{\Delta}) = W(\boldsymbol{\Delta})\big|H(\boldsymbol{\Delta})\big|^2. \tag{13.22}$$

To generate lumpy backgrounds of type II with the same autocorrelation function as lumpy backgrounds of type I, we define $H(\boldsymbol{\Delta})$ as

$$H(\boldsymbol{\Delta}) = H(0)\exp\big(-\pi^2 r_b^2|\boldsymbol{\Delta}|^2\big), \tag{13.23}$$

where $H(0)$ is the amplitude of the filter and r_b is the correlation length of the resulting autocorrelation function. The filtered power spectrum is then given by

$$W_f(\boldsymbol{\Delta}) = W(0)\big[H(0)\big]^2\exp\big(-2\pi^2 r_b^2|\boldsymbol{\Delta}|^2\big). \tag{13.24}$$

The expression for the autocorrelation function is then given by the inverse Fourier transform of the power spectrum as

$$R_f(\mathbf{r}) = \frac{W(0)[H(0)]^2}{2\pi r_b^2}\exp\left(-\frac{|\mathbf{r}|^2}{2r_b^2}\right). \tag{13.25}$$

The measure of lumpiness is now given by

$$W_f(0) = W(0)\big[H(0)\big]^2, \tag{13.26}$$

where $H(0)$ is simply a number and $W(0)$ is in units of counts per unit time and per unit area. Therefore, $W_f(0)$ is again in units of counts^2/(s^2 mm^2) for example. In the case of discretization of all quantities for digital simulations, $W_f(0)$ will be expressed in units of counts^2/(s^2 pixel).

13.3.6 Examples of lumpy backgrounds type I and II

Examples of lumpy backgrounds of types I and II are shown in Figure 13.9(a) and (b), respectively. In Figure 13.9(a), the mean background $\overline{B}$ increases from left to right with values of 384, 1664, and 3200 counts/(s pixel), and the lumpiness increases from top to bottom with $W_f(0)$ equals 10^4, 10^5, and 10^6 counts^2/(s^2 pixel). As the lumpiness increases, the strength of the blobs b_0 increased from 1280, 4047, and 12,800 counts/s, while the mean number of blobs is 100. In Figure 13.9(b), the value of $\overline{B}$ and $W_f(0)$ are the same as in Figure 13.9(a). As the lumpiness increases, the variance of the noise increases with σ equal 33.33, 105.41, and 333.33 pixels, respectively. As $\overline{B}$ increases, the strength of the filter takes the values 3, 13, and 25, respectively.

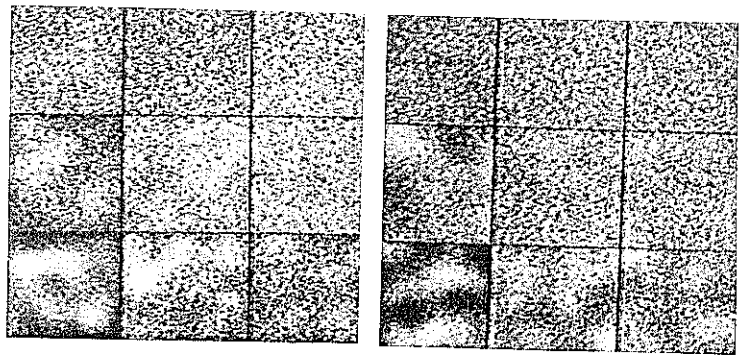

(a) (b)

Figure 13.9: (a) Lumpy backgrounds of type I. (b) Lumpy backgrounds of type II.

13.4 Modeling liver scans

Cargill (1989) proposed a computer-generated 3D model of liver with the possibility to include various disease states [22]. Such a model, when combined with a model of imaging in nuclear medicine, was applied to imaging-system design optimization. Specifically, Cargill investigated the correlation of the Hotelling observer (presented in Chapter 11 of this book in the context of lumpy backgrounds) with human performance for nine different systems. This study was one of the milestones in showing that the Hotelling observer can be used to predict human performance.

Cargill also investigated how changes in texture correlated with disease states. In such investigation, the aim was to establish quantitative measures of the power spectrum of livers independently of the imaging system. Cargill estimated the contribution of the imaging system to real scans, and used the mathematical liver model to validate the approach. This investigation was one step forward in the development of imaging systems designed to optimize the amount of information related to, in this case, the texture associated with the liver being imaged. The methods may apply equally well to other organs [23].

Modeling the liver includes defining its three-dimensional shape and filling its volume. Object classes of normal livers were constructed by randomly perturbing the surface of the normal liver.

Liver diseases may be classified as focal or diffuse. Focal lesions correspond to reduced uptake of tracer in the liver. Focal lesions are typically liver tumors, metastatic lesions, and inflammatory disease such as amebic abscesses. In the case of diffuse disease, the entire liver structure is altered. Liver diseases were modeled to represent tumors, metastatic disease, and forms of inflammatory and diffuse diseases that we shall summarize here [22].

13.4.1 Modeling the shape of the liver

In modeling the shape of the liver, it was assumed that the surface of the liver could be expressed as an analytic function of vectors drawn from the origin of a coordinate system to points on the surface of the liver. This function was obtained from a set of measurements of points on the surface of a normal liver. The sampled function was then expanded in a set of orthogonal basis functions which spanned its vector space [24]. The three-dimensional fitted liver is then constructed by placing it at the center of a 3D grid attached to a coordinate system. The space is then divided into equal volume elements, or voxels. If a voxel is established to be inside the liver volume, the voxel is assigned a constant value that represents in nuclear medicine the uniform uptake of tracer throughout normal liver tissue.

In mapping the surface of the liver, because the liver appeared to possess approximate symmetry relative to spherical coordinates, the measurement data set acquired was mapped in a spherical polar coordinate system. The data set will be denoted $f(\theta, \phi)$. Spherical harmonics, denoted $Y_{lm}(\theta, \phi)$ are given by

$$Y_{lm}(\theta, \phi) = (-1)^m \sqrt{\frac{2n+1}{4\pi} \frac{(n-m)!}{(n+m)!}} P_{lm}(\cos\theta) e^{im\phi}, \tag{13.27}$$

where l and m are integers to keep the functions single valued, $-l \leqslant m \leqslant l$, and $P_{lm}(\cos\theta)$ are the associated Legendre polynomials given by

$$P_{nm}(x) = \frac{1}{2^n n!}(1-x^2)^{m/2} \frac{d^{m+n}}{dx^{m+n}}(x^2-1)^n. \tag{13.28}$$

Because the spherical harmonics are orthonormal and complete, any single-valued function of θ and ϕ evaluated over the surface can be expanded in a uniformly convergent double series of spherical harmonics, a Laplace series,

$$f(\theta, \phi) = \sum_{l=0}^{\infty} \sum_{m=-l}^{l} a_{lm} Y_{lm}(\theta, \phi). \tag{13.29}$$

If $f(\theta, \phi)$ is known, the expansion coefficients a_{lm} are determined by evaluating the product of the function to be fitted with the corresponding spherical harmonic over the unit sphere

$$a_{lm} = \int_0^{2\pi} \int_0^{\pi} Y_{lm}^*(\theta, \phi) f(\theta, \phi) \sin\theta \, d\theta \, d\phi, \tag{13.30}$$

where the asterisk denotes the complex conjugate. Once the expansion coefficients have been determined, the function $f(\theta, \phi)$ can be reconstructed using the spherical harmonics.

In practice, the function $f(\theta, \phi)$ is sampled at discrete values of θ and ϕ, denoted θ_k and ϕ_n, given by

$$\theta_k = \frac{k\pi}{K}, \qquad \phi_n = \frac{2n\pi}{N}. \tag{13.31}$$

The sampled spherical harmonics $Y_{lm}(\theta_k, \phi_n)$ are not in general orthogonal and therefore

$$\sum_{k=1}^{K} \sum_{n=1}^{N} Y_{l'm'}^*(\theta_k, \phi_n) Y_{lm}(\theta_k, \phi_n) = \varepsilon_{l'm'lm}, \tag{13.32}$$

where $\varepsilon_{l'm'lm}$ can be considered a nonzero residue. The residue does not allow the double sum over l and m to be eliminated, and the calculation of one expansion coefficient cannot be isolated from the others. As the values of K and N become large, the residue becomes negligible, and the contribution of the coefficients where $l' = l$ and $m' = m$ are acceptably small.

There are useful recursion relations that relate adjacent values of l and m in the associated Legendre polynomials contained in the spherical harmonics [25]. These recursion relations facilitate calculating the spherical harmonics up to any desired value of l, once the few lowest-order terms have been computed, without having to perform the multiple differentiations that occur in the definition of the associated Legendre polynomials. The recurrence formula relating adjacent values of l is given by

$$P_{l+1,m}(x) = \frac{2l+1}{l-m+1} x P_{lm}(x) - \frac{l+m}{l-m+1} P_{l-1,m}(x). \tag{13.33}$$

The expression relating adjacent values of m is given by

$$P_{l,m+1}(x) = \frac{-2mx}{(1-x^2)^{1/2}} P_{lm}(x) - (l+m)(l-m+1) P_{l,m-1}(x). \tag{13.34}$$

There is also an expression relating spherical harmonics with index $-m$ to those with index m given by

$$Y_{l,-m}(\theta, \phi) = (-1)^m Y_{lm}^*(\theta, \phi). \tag{13.35}$$

Each expansion coefficient can then be calculated directly once the corresponding spherical harmonic term has been established. The surface of the liver can then be reconstructed from typically a truncated set of the spherical harmonics.

An ensemble of normal livers can be generated efficiently by perturbing randomly the spherical harmonics coefficients, from which new livers may be reconstructed. In doing so, the basic shape of the liver remains unchanged but the changes introduced represent normal size and shape variations.

13.4.2 *Examples of mathematically fitted liver*

For the case of the liver modeled by Cargill, the function $f(\theta, \phi)$ was typically sampled over 24 values of azimuthal angle ϕ (every 15°) and 36 values of polar angle θ (every 5°), giving a total of 840 values. For an expansion up to $l = 7$, the largest residue was 0.001, considered negligible. In the case of coarser sampling, where the residue cannot be ignored, a Schmidt orthogonalization procedure on the spherical harmonics allows creation of a new set of functions composed of

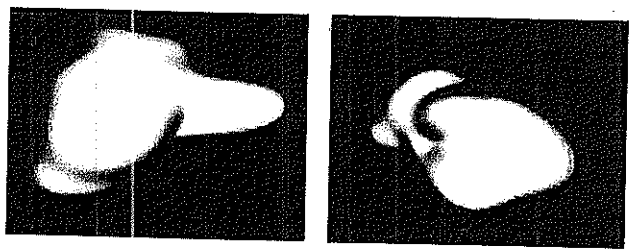

(a) (b)

Figure 13.10: Simulation of a mathematically fitted liver scan (a) anterior view and (b) right lateral view (courtesy of Ellen Cargill, 1989).

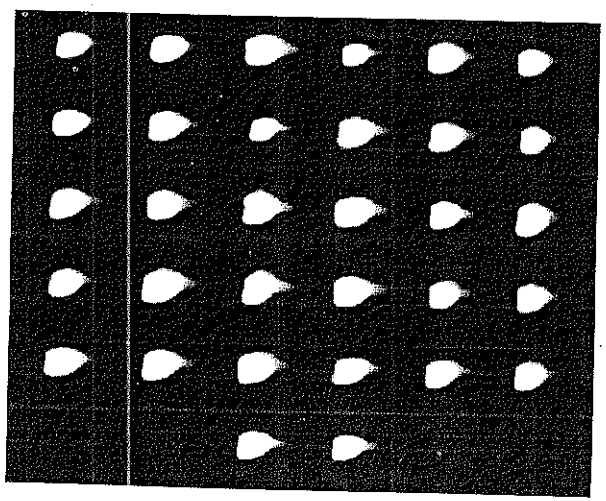

Figure 13.11: In this figure, 32 normal livers obtained from perturbing randomly the spherical harmonics coefficients are displayed (courtesy of Ellen Cargill, 1989).

weighted sums of the spherical harmonics that will be closer to being orthogonal over the sample space [25]. Figure 13.10 depicts shaded representations of an anterior view and a right lateral view of the mathematically fitted liver. Figure 13.11 shows two-dimensional projections of 32 normal livers created by perturbing randomly the spherical harmonics coefficients.

13.4.3 *Modeling focal liver disease*

Disease that is local in nature is referred to as focal disease. The most common primary focal liver tumor is hepatoma. Such lesions were modeled as ellipsoids within the liver parenchyma having uptake equal to 10% of normal liver tissue. Simulated lesions were located randomly within the liver volume.

13.4.4 *Modeling metastatic disease*

A major function of the liver is to process blood coming from the digestive system. Thus the liver is likely to track metastatic cells originating from the digestive system because of its proximity and the fact that it is the first extensive capillary network the cells encounter. If the liver fails to destroy these cancer cells, they may further metastasize. Consequently, the liver has a high rate of involvement in metastatic disease. Metastatic lesions can be modeled as multiple cold ellipsoids randomly located and oriented to represent lesions of various sizes randomly located within the liver volume.

Hepatomegaly, which is the enlargement of the liver, often accompanies the development of metastatic disease and is modeled by scaling the liver uniformly by multiplying the spherical harmonic coefficients by a constant.

13.4.5 *Modeling inflammatory disease*

Inflammation of the liver may be a response to infection. If the infection is focal in nature, such as an abscess, then the inflammation is likely to be focal in nature. In this case, cold ellipsoids randomly localized in the volume of the liver may be used to model abscesses. However, inflammation may also be associated with viral hepatitis, in which case the inflammation will be generalized and be modeled as diffuse disease.

13.4.6 *Modeling of diffuse disease*

Diseases that affect the overall parenchyma of the liver are referred as diffuse disease. Hepatitis and cirrhosis are common examples. The development of cirrhosis follows the self-similar structure of the liver. Rappaport *et al.* (1983) identified three basic types of lesions based on the degree of involvement of the higher orders of parenchyma organization [26]. They suggested to classify nodules based on their state of vascularization, which lead to defining triadal, paratriadal, and atriadal nodules. In addition, changes that may occur in the liver include hepatomegaly, left-lobe hypertrophy, righ-lobe blunting, heterogenous uptake, and low overall uptake. Other features related to the spleen and the vertebral bone marrow may also be present to some degree.

Changes in morphology of the liver may manifest as hepatomegaly or atrophy, or local enlargement. Atrophy can be modeled by altering the original data set representing the surface and refitting the deformed surface by a set of new coefficients. This perturbation involves varying the points on the modeled surface over some angular range. Most importantly, the data set must be perturbed in a smooth fashion to ensure a good fit of spherical harmonics to the perturbed data set [22]. Given a deformed liver, an ensemble may be simulated by varying the spherical harmonics coefficients.

Heterogenous uptake in the liver occurs frequently in cirrhosis of the liver. Such uptake manifests as a patchy appearance of the liver or texture. This is the result of portions of the liver parenchyma being replaced by scar tissue, and consequently not taking up any of the tracer. Patchy uptake was simulated by using a 3D texture in the volume of the liver. A 3D texture was obtained by filtering white noise in the Fourier domain with a $1/f^n$ spectrum. We shall further address more advanced methods for texture synthesis in Section 13.6.

13.5 Synthesizing ultrasound B-scan images

Pioneer work in texture synthesis for image-quality assessment in medical imaging can be found in ultrasound imaging. The need for synthetic images in ultrasound imaging first arose from the need to test novel methods for processing ultrasound signals [27]. Fink (1983) investigated the use of short-time Fourier analysis to provide an estimation of the echographic spectral composition as a function of time. Simulated echographic data from a one-dimensional tissue model was used to test this new method.

Insana *et al.* (1986) investigated how tissue signatures may be obtained from first and second-order statistics of ultrasonic B-scan textures [28]. In order to isolate second-order statistics, they identified nonstochastic stuctures in Rician noise fields such as blood vessels. The identification was established by thresholding a correlation image obtained from using a matched-filter technique in which a one-dimensional function is cross-correlated with the ultrasound image. Correlation thresholds were established by studying simulated images with known statistics. In another related investigation, Wagner *et al.* (1986) simulated images with Rician statistics and presented an algorithm for automatically ranking the images based on their statistical properties [29].

Momenan *et al.* (1988) employed simulated ultrasound B-scan-like images to establish which statistical parameters were most useful in discriminating tissue types. The main use of synthetic images was in the validation of image-processing techniques [30].

Finally, Valckx and Thijssen (1997) investigated the potentials of co-occurrence matrix analysis for the characterization of echographic image textures [31]. They simulated one-dimensional data sets with different number densities of the randomly distributed scatterers, and with different levels of structural scattering strength.

13.5.1 Modeling ultrasound B-scan images

The scattering of a radio-frequency (rf) wave from a random medium such as soft tissue involves a random walk in two dimensions corresponding to the real and imaginary components of the rf signal [32, 33]. Ultrasonic backscattered or echo pulses from soft tissues, when displayed as a clinical B-scan image, form a texture pattern that is characteristic of both the imaging system and the tissue being imaged [34]. The resulting images have the granular structure described as texture or speckle, which results from interactions (i.e., absorption, reflection, scattering) between the coherent ultrasonic pulses transmitted into the body and the microscopic (0.008 mm to 2 mm) structures of the tissue [35]. Scattering, responsible for the random character of the images, occurs at multiple sites randomly distributed within the resolution cell of the ultrasonic transducer.

Histological studies have shown that tissue scatterers vary in size and shape and that the different structures have varying degrees of spatial order. The organization of scattering stuctures for most biological media falls somewhere between blood, which is completely disordered and consists of randomly distributed scatterers, and skeletal muscle tissue, which is highly ordered with nearly periodic scatterers that repeat over a long range [36].

In the synthesis of ultrasonic B-scan texture images, soft tissues may be represented as an acoustically uniform medium that comprises two different classes of scatterers [29]. In this modeling approach, the first class of scatterers consists in randomly positioned scatterers according to a uniform distribution. This scatterer class corresponds to diffuse scatterers within tissue. The process of interference for the diffuse component can be geometrically described as a random walk of component phasors and the received complex signal such as the rf voltage output V_d of the ultrasound transducer can be modeled as the sum of N complex signals from individual identical discrete scatterers

$$V_d = \sum_{j=1}^{N} a_j = \sum_{j=1}^{N} |a_j| \exp(i\phi_j) = a_{dr} + ia_{di}, \tag{13.36}$$

where the index d denotes the diffuse component, the index r and i denote the real and imaginary parts, respectively, and N represents the number of scatterers per resolution cell.

The second class of scatterers consists in nonrandomly distributed scatterers with long-range order. This can be modeled by adding a complex signal to the random sum, represented most generally as a phasor of real component a_{sr} and imaginary component a_{si}. The quantity $I_s = (a_{sr}^2 + a_{si}^2)$ is referred to as the specular intensity. Because this specular contribution is distributed over a region of the tissue or source of scattering, it is referred to as distributed specularity. The output voltage V is in this case given by

$$V = (a_{sr} + ia_{si}) + (a_{dr} + ia_{di}). \tag{13.37}$$

Examples of specular scatterers in tissues with resolvable long-range order are the portal triads and lobules in liver parenchyma and the collagenous sheaths that surround muscle bundles. Structures such as blood vessels and organ surfaces are not considered part of the texture, and are thus not included in this ultrasound texture model.

13.5.2 *First and second-order statistics of ultrasound images*

The first-order statistics are determined by the gray-level histogram of the B-scan or magnitude image. Considering first the diffuse scatter component, when the number of scatterers within a resolution cell is large and the phases of the scattered waves are independent and distributed uniformly between 0 and 2π, the complex amplitude V_d resulting from the random walk has real and imaginary components a_{dr} and a_{di} whose joint probability density function (pdf) is a circular Gaussian given by

$$\mathrm{p}(a_{dr}, a_{di}) = \frac{1}{2\pi\sigma} \exp\left[-\left(a_{dr}^2 + a_{di}^2\right)/2\sigma^2\right]. \tag{13.38}$$

This is simply the product of two independent Gaussian density functions with zero mean and variance that can be shown to depend on the mean-square scattering amplitude of the particles in the scattering medium [37]. The average incoherent backscattered intensity component represented as the mean square of the complex amplitude averaged over all particles in the scattering medium is given by

$$\langle V_d V_d^* \rangle = \left\{a_{dr}^2 + a_{di}^2\right\} = 2\sigma^2 = I_d, \tag{13.39}$$

and will be referred to as the mean diffuse intensity I_d. The pdf associated with $|V_d| = \sqrt{I_d}$ can be shown to follow a Rayleigh pdf, while the pdf associated with $|V_d|^2 = I_d$ is an exponential pdf. The magnitude $\sqrt{I_d}$ is the quantity of interest, as ultrasound B-scan displays the envelope of the echo of the received signals, and the envelope is the instantaneous value of the magnitude of the phasor when the signal is sufficiently narrowband [33].

When the distributed specular component is also considered, the joint pdf of the real and imaginary components a_{dr} and a_{di} then becomes

$$\mathrm{p}(a_{dr}, a_{di}) = \frac{1}{2\pi\sigma^2} \exp\left[-\left((a_{dr} - a_{sr})^2 + (a_{di} - a_{si})^2\right)/2\sigma^2\right], \tag{13.40}$$

where Eq. (13.37) was considered. The pdf associated with $|V|$ when both diffuse and specular reflections are considered, can be shown to follow a Rician probability density function generalized to include a spatially structured specular signal [32].

Wagner *et al.* (1983) found that the most fruitful second-order measure for analyzing ultrasound textures was the autocorrelation function and its Fourier transform, the texture power spectrum [38]. They have derived them, using the analytical apparatus of Middleton (1960), for the cases of the signal amplitude and signal intensity. They found that the straightforward study of the intensity signal led to the same results that follow from the more complicated envelope analysis [39]. The results for intensity are thus reported in this chapter.

The average correlation between one intensity measurement I at position x, and another measurement, I' at position $x' = x + \Delta x$, where the second measurement is obtained by translating the transducer a fixed distance Δx, can be shown to reduce to

$$\begin{aligned}\langle II' \rangle &= I_d^2\left(1 + |\rho|^2\right) + I_d(I_s + I_s') + \left\{(I_s \otimes I_s')\right\} + 2I_d\rho\left\{(a_{sr} \otimes a_{sr}' + a_{si} \otimes a_{si}')\right\} \\ &= I_d^2\left(1 + |\rho|^2\right) + 2I_d\left(\overline{I_s}\right) + \left\{(I_s \otimes I_s')\right\} \\ &\quad + 2I_d\rho\left\{(a_{sr} \otimes a_{sr}' + a_{si} \otimes a_{si}')\right\},\end{aligned} \tag{13.41}$$

where the angle brackets denote expectation value, the symbol $\otimes$ indicates the conventional correlation operation, and $\langle\otimes\rangle$ further denotes the correlation operation averaged over the record length X of the position variable x. Also, the parameter ρ is the complex coherence factor (i.e., normalized autocovariance of the complex field) defined as

$$\rho = \langle V V'^* \rangle / \sqrt{\left\{|V|^2\right\}\left\{|V'|^2\right\}}. \tag{13.42}$$

The Fourier transform of the autocorrelation function yields the expression for the power spectrum detailed in Wagner *et al.* (1987) [39].

13.5.3 *Examples of simulated ultrasound B-scan images*

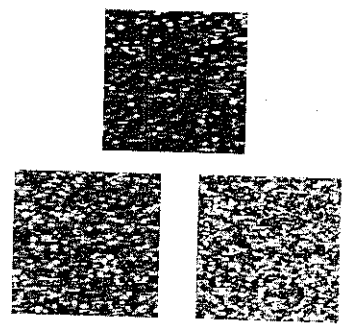

Figure 13.12: Sample images of ultrasound Bscans generated by computer simulation. The top images corresponds to fewer than 1 scatterer per resolution volume. The lower left and right images correspond to 2 and 6 scatterers per resolution volume, respectively. (Courtesy of Robert Wagner, FDA, Maryland.) (Copyright 1997, American Institute of Physics [62].)

13.6 Texture synthesis

In the same way that patchy uptake in the liver may be represented as a texture [22, 28], other medical images such as parenchyma in breast tissue and the inner structure of bones, may also be modeled as textures [40, 41]. Abnormality in the breast tissue parenchyma may manifest itself as architectural distortions in mammography for example. Loss in bone strength, generally with aging, is known as osteoporosis. Osteoporosis can be diagnosed from loss in bone density, yet the change in structure itself, while harder to measure is also thought to be important to establishing the state of disease and the effectiveness of drugs, for example, to rebuild bone strength [42].

Texture synthesis is the ability to create, from one acquired texture sample, an ensemble of images that look visually similar in structure, yet differ pixel to pixel from the acquired sample. As pointed to earlier in this chapter, the importance of synthesized textures in the assessment of image quality in medical imaging lies in the ability to be able to generate large ensembles of statistically equivalent images [43]. These images may serve as background images into which one may or may not insert objects of interest (i.e., lesions), or may serve as the object of interest itself [44]. Such statistically equivalent ensembles provide an effective means to assess image quality in medical systems such that findings will more easily transfer to clinical images.

13.6.1 General method of texture synthesis

Various natural textures have been effectively synthesized using a multi-layer pyramid transform that allows decomposition of a sample image at different scales and orientations [45]. After decomposition of a sample image, the histograms of the subimages thus obtained were employed to modify the histogram of a uniformly distributed white noise image that had been submitted to the same decomposition. The reconstruction, or synthesis, of the modified noise subimages yields a synthesized texture. Each new synthesis requires a new realization of the noise image.

13.6.2 Pyramid transform and image decomposition

An n-layer steerable pyramid transform constitutes the basis for the texture synthesis algorithm. One layer of the pyramid is depicted in Figure 13.13. Layers are connected by a factor of two *decimation*, of the image [46]. Decimation is a downsampling operation that consists in retaining every other pixel in an image. It is applied after low-pass filtering of the image, represented as "blur filter" on the left-hand side of the pyramid. Within each layer, the image is then filtered by a set of bandpass filters and followed by a set of orientation filters that form a quadrature mirror filter bank [47–50]. Four scales and four orientations 17×17 size filters, corresponding to 0-degree, 45-degree, 90-degree, and 135-degree orientations, were adopted in the simulation shown here.

During the decomposition synthesis, the sample texture image is processed through the left-hand side of the pyramid. It is represented in Figure 13.13 as an

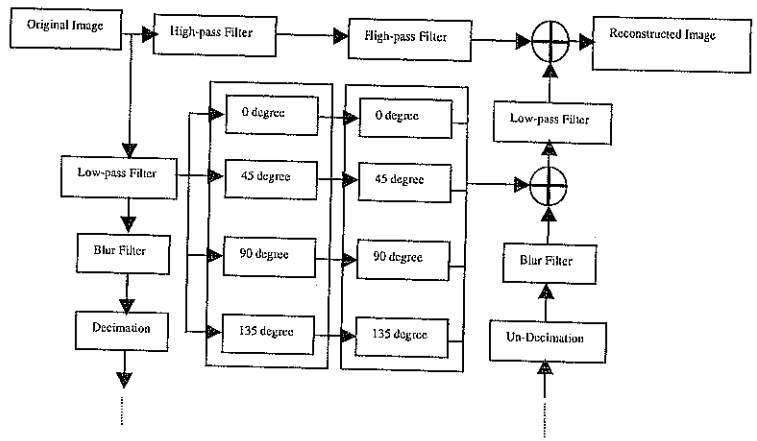

Figure 13.13: A layer of the steerable pyramid transform employed in the texture synthesis algorithm is shown. The image in the upper-right corner is either a texture sample or a realization of a white noise. The left hand of the pyramid is used for decomposing the two images. The right-hand side of the pyramid is used for image reconstruction or synthesis.

input to the pyramid in the upper left corner. In parallel, a realization of uniformly distributed white noise is processed through the same pyramid. The role of the white noise image is to provide a starting point for the synthesis.

13.6.3 Histogram matching and synthesis

The method of texture synthesis employs a technique known as histogram matching of two images. Histogram matching, sometimes referred to as histogram specification, is an image processing technique, specifically a point operation, which modifies a candidate image so that its histogram matches that of a model image [51]. While histogram matching is not widely employed in image processing, it is a generalization of histogram equalization, an image processing technique commonly employed to enhance low-contrast images [52–54].

The histograms of the subband noise images at multiple scales and multiple orientations are then matched to the corresponding histograms of the subband sample images. Fast algorithms for histogram matching have been proposed and investigated for enhancing the efficiency of the synthesis process [55]. Efficiency of the histogram matching operations is important in texture synthesis because the operations of decomposition and histogram matching are performed recursively, where the first synthesized image serves as the input noise image in the second iteration of the algorithm. While a quantification of the optimal number of iterations is subject to current investigation, five to seven iterations are typically performed.

The modified subband noise images are then recombined according to the right-hand side of the steerable pyramid transform shown in Figure 13.13. Starting from the lowest layer, images are undecimated from layer to layer. Undecimation is an upsampling operation that consists in inserting zero values in between pixels of the image. Such operation is followed by a blurring of the image represented as "blur filter" on the right-hand side of the pyramid. Moreover, at each upsampling operation, the intensity values are multiplied by four to compensate for the loss in image brightness that resulted during the downscaling of the images during the decomposition phase [43].

13.6.4 A two-component decomposition approach

The approach to texture synthesis described was extended to synthesize medical images such as mammograms [41]. The key to the successful synthesis of such images was an additional decomposition of the sample texture image into two components: the larger spatial variations in the image and a smaller relative scale underlying texture, shown in the upper-right and lower-left corners of Figure 13.14,

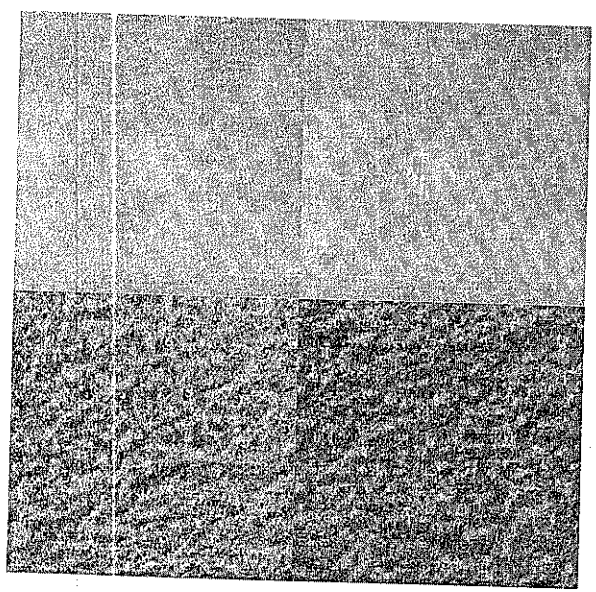

Figure 13.14: A segment of a mammographic image is shown in the upper-left corner. The extracted larger scale component is shown in the upper-right corner. The relatively smaller-scale component is shown in the lower-left corner. Finally a synthetic realization of the smaller-scale component is shown in the lower-left corner.

respectively. The larger scale images are reminiscent of lumpy images described earlier. One realization of the synthesized smaller scale texture is also shown in the lower right corner of the figure.

13.6.5 A breast-tissue mathematical phantom

The synthesis of an ensemble of images $M_i(x, y)$ can be established using an adaptive linear combination of realizations from the two model components: a realization of a broadly spatially varying texture, such as a lumpy image, denoted as $L_i(x, y)$, and a realization of the synthesized underlying texture component denoted as $T_i(x, y)$. The resulting synthesized image is then given by

$$M_i(x, y) = \alpha L_i(x, y) + (1 - \alpha) T_i(x, y), \tag{13.43}$$

where α ranges from 0 to 1. Such a combination allows spanning of a wide range of tissue types with relative amounts of the broadly spatially varying component and the smaller-scale texture component. Such an approach to the synthesis of medical images may naturally find application to other types of images beside mammographic tissue.

13.6.6 Computation of first- and second-order statistics of synthetic textures

The first-order statistics of synthetic textures is the gray-level histogram of the sample texture employed in the synthesis given that histogram matching is part of the synthesis process, and it is also performed as a last step of the synthesis.

For Gaussian random processes, such as the lumpy backgrounds described earlier, the autocorrelation function or equivalently the power spectrum fully characterizes the second-order statistics. Knowledge of the first-order statistics and the autocorrelation function are in fact sufficient to compute the statistical properties of the random process to any order.

For non-Gaussian random processes, the complete second-order statistics are defined as the two-point probability density function (2P-PDF) also known as the co-occurrence matrix, especially in the literature on image processing. Julez first used gray-tone spatial dependence co-occurrence statistics in texture discrimination experiments [56].

A component of the complete 2P-PDF is computed as the frequency of simultaneous occurrence of two gray levels from two pixels separated by a directional distance $\mathbf{d}$ [60]. As $\mathbf{d}$ varies in size and orientation, the complete 2P-PDF is formed. A few components of the complete 2P-PDF for the small-scale mammographic texture are shown in Figure 13.15. Both components of the 2P-PDF of the original texture (i.e., left image) and a synthetic realization of the same texture (i.e., right image) are shown. Specifically, components of the 2P-PDF for values of $\mathbf{d}$ equal $(-5, -5)$, $(-3, -5)$, $(3, -5)$, and $(5, -5)$ from upper left to right, and $(-5, -5)$, $(-5, -3)$, $(-5, 3)$, and $(-5, 5)$ from top left to bottom left are presented. For each component shown, the co-occurrence of two gray levels varying between 0–255 is coded as intensity values.

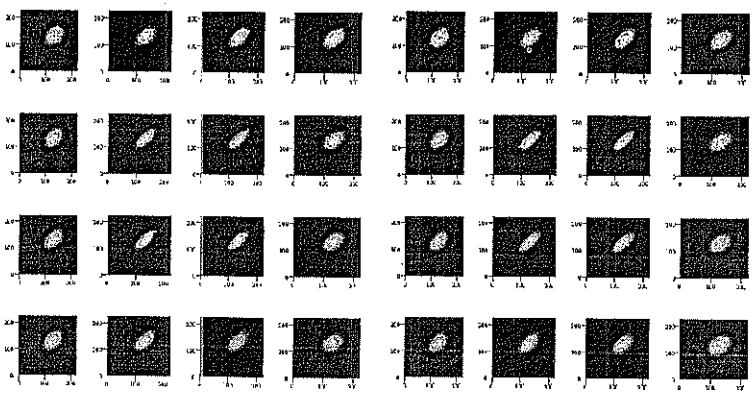

Figure 13.15: On the left, components of the 2P-PDF of the small-scale mammographic texture image are shown for values of $\mathbf{d}$ equal $(-5,-5)$, $(-3,-5)$, $(3,-5)$, and $(5,-5)$ from upper left to right, and $(-5,-5)$, $(-5,-3)$, $(-5,3)$, and $(-5,5)$ from top left to bottom left. On the right, the same components for a synthetic realization of the texture are shown. On each component, the co-occurrence of two gray levels varying between 0–255 is coded as intensity values.

Given that computing the complete 2P-PDF is quite demanding, various statistical measures have been extracted from the 2P-PDF for use in automatic texture discrimination [57]. The autocorrelation function or equivalently the power spectrum, for example, have been some of the measures most widely employed in analyzing statistical images like natural scenes. While the fact that the power spectra of natural images such as textures follow some power law may be found to be significant, it is important to note that power spectra do not provide complete descriptors of second-order statistics if the process is non-Gaussian. The power spectrum can be computed from the 2P-PDF but the reverse is not true.

Importantly, specifically two studies demonstrate that two sets of images with equal power spectra, yet having Fourier spectra that differ in phase, yield different detectability performance for human observers [58, 59]. In both investigations, ensembles of images with their natural noise, and ensembles of images with their natural-phase spectra replaced with random-phase spectra were considered in the study. Furthermore in Bochud (1995), ensembles of images with equal power spectra but with Fourier spectra of different phases were obtained by filtering various realizations of white noise with the desired power spectrum. Bochud considered a location know-exactly detection task, where human subjects were asked in a two-alternative forced choice experiment which image contained a small object. The object to be detected was six pixels in size in a 256×256 image, and aimed at simulating microcalcifications in mammography. Thomson (1997) looked at the ability to visually discriminate between two textures presented in a temporal-sequential

paradigm. These investigations pointing to the importance of the phase spectra of texture images document the importance of looking at the complete second-order statistics, not simply the power spectra, to characterize texture images and quantify task performance in textured images.

It must be noted that the first-order statistics have a significant impact on the form of the 2P-PDF. In the limit of large $\mathbf{d}$ values, the 2P-PDF becomes the product of the 1P-PDFs, that is the first-order statistics or histograms. Thus, if textures are compared based on their second-order statistics, they must be first equaled in first-order statistics. Harris (1999) investigated histogram matching to either a uniformly distributed random process, which is equivalent to histogram equalization, or a Gaussian distribution [61]. After equalization of first-order statistics, a simple distance measure was computed between two 2P-PDFs as

$$D(p^a, p^b) = \frac{1}{N_{\mathbf{d}}} \sum_{\mathbf{d}} \left(\sum_{ij} \left[p^a(\mathrm{GL}_i, \mathrm{GL}_j; \mathbf{d}) - p^b(\mathrm{GL}_i, \mathrm{GL}_j; \mathbf{d}) \right]^2 \right)^{1/2}, \quad (13.44)$$

where ij is a pair of gray levels, p^a and p^b are the 2P-PDFs for texture a and b, respectively, and $N_{\mathbf{d}}$ is the number of directional distances considered. Other distance measures that may provide enhanced classification are currently subject to investigation.

Based on the distribution of distance values within ensembles of texture images, and the mean distance values across different ensembles of texture images, Harris found higher performance for texture discrimination in the case of matching to a Gaussian distribution. Optimization of the Gaussian parameters for specific medical data sets may provide improved means of texture classification based on the complete 2P-PDF.

For the problem of texture classification, a crucial part of the classification algorithm is the estimation of the 2P-PDF for a given texture realization. While the simplest way to estimate a 2P-PDF is the relative-frequency method, it generally yields noisy estimates. A question is how many sample points should be considered to estimate a probability density function with known accuracy using the relative-frequency method? An estimate based on the maximum-entropy (ME) method, where moments of the random process are used to constrain the estimate, yields smoother estimates. Similarly, one must ask in this case how many moments should be considered? The problem of 2P-PDF estimation was investigated an reported in Goon and Rolland (1999) [60]. Results show that the maximum-entropy method yields accurate estimates, however efficient computational methods must be investigated.

13.7 Conclusion and future work

Mathematically synthesized images have played and will continue to play an important role in deepening our understanding of images and in quantifying image quality in medical imaging. Computer-simulated angiograms, lumpy backgrounds,

and the synthesis of 3D livers, ultrasound B-scans, and mammographic textures were reviewed.

The ability to simulate angiograms allowed researchers to investigate the role of blood-vessel curvature in the detection of lesions, as well as the impact of structural context near lesions. Furthermore, it allowed controlled experiments where detectability in a search experiment could be investigated, given that the detectability in the location-known-exactly task could be measured and set equal across the conditions investigated for the search experiment. The simulations thus allowed for designing experiments that would not be realizable using clinical images.

The ability to simulate images with spatially varying components, yet well defined statistics, as found in the lumpy backgrounds, allowed us to model detection of lesions in spatially varying backgrounds often encountered in medical images. The use of spatially varying backgrounds, rather than previously chosen constant backgrounds, allowed researchers to resolve the long existing paradox between predictive models of detection and clinical experience. It also allowed further test of the validity of observer models, reported in another chapter of this book, to predict human performance in various classification tasks.

A method for the simulation of organs was presented. The application to modeling liver scans was shown as well as the ability to model various liver diseases. Such mathematical phantoms played an important role in demonstrating the ability of the Hotteling observer to predict human performance in a classification task.

Finally, methods for synthesizing texture images were presented including the synthesis of ultrasound B-scan images, and the synthesis of mammographic textures. The goal of texture synthesis is to render an ensemble of images with statistical properties that are equivalent to those encountered in clinical images. The complete 2P-PDF is considered a meaningful measure of second-order statistics of texture images for non-Gaussian random processes.

Lumpy backgrounds, ultrasound B-scan modeling, and mammographic-tissue synthesis constitute pioneer work in the modeling of texture images. Extensive work is yet to come to investigate and compare various approaches to texture synthesis for medical imaging, establishing efficient methods to estimate 2P-PDFs for effective texture characterization, and further validating the ability to effectively classify medical textures based on second-order statistics as well as possibly higher-order statistics. Moreover, statistical models of medical textures may be employed in establishing priors for image reconstruction.

Finally, in the same manner that we simulated lumpy backgrounds based on wanting to render texture images with a given autocorrelation function, methods to synthesize textures that satisfy specific predefined statistics may provide a useful tool to the field of image understanding and quality assessment in medical imaging.

Acknowledgments

I thank Kyle Myers for her inputs in presenting this material and for her kind review of the manuscript and suggestions. I am thankful to Harry Barrett for providing original pictures regarding the synthesis of liver scans, but most importantly for providing me with a vision and continued encouragement that inspires me always. Finally, I thank Keith Wear and Robert Wagner for their inputs on the section on synthesizing ultrasound B-scans and providing an illustration as well.

References

[1] Swets JA. "Measuring the Accuracy of Diagnosis Systems." Science 240:1285–1293, 1988.

[2] Barrett HH, Yao J, Rolland JP, Myers KJ. "Model Observers for Assessment of Image Quality." Proc Natl Acad Sci 90:9758–9765, 1993.

[3] Revesz G, Kundel HL, Graber MA. "The Influence of Structured Noise on Detection of Radiologic Abnormalities." Invest Radiol 9:479–486, 1974.

[4] Tobis J, Nalcioglu O, Iseeri L *et al.* "Detection and Quantitation of Coronary Artery Stenoses from Digital Substraction Angiograms Compared with 35 Millimeter Film Cineangiograms." Am J Cardiol 54:489–496, 1984.

[5] Davatzikos C. "Spatial Transformation and Registration of Brain Images Using Elastically Deformable Models." Comp Vis and Image Understanding, Special Issue on Medical Imaging 66(2):207–222, 1997.

[6] Rolland JP, Muller K, Helvig CS. "Visual Search in Medical Images: A New Methodology to Quantify Saliency." Proc SPIE 2436, 1995, pp. 40–48.

[7] Rolland JP, Helvig CS. "Visual Search in Angiograms: Does Geometry Play a Role in Saliency?" Proc SPIE 2712, 1996, pp. 78–88.

[8] Puff D. "Human Vs. Vision Model Performance for Two Medical Image Estimation Tasks." Ph.D Dissertation, University of North Carolina at Chapel Hill, 1995.

[9] Rolland JP, Puff D. "Angiogram Simulation Software Documentation." Technical Report TR93-018, University of North Carolina at Chapel Hill, 1993.

[10] O'Neill Barrett. *Elementary Differential Geometry*. Orlando: Academic Press, 1966, p. 75.

[11] Tsui BMW, Metz CE, Atkins FB, Starr SJ, Beck RN. "A Comparison of Optimum Spatial Resolution in Nuclear Imaging Based on Statistical Theory and Observer Performance." Phys Med Biol 23:654–676, 1978.

[12] Wagner RF, Brown DG, Metz CE. "On the Multiplex Advantage of Coded Source/Aperture Photon Imaging." In Brody W (Ed.) *Digital Radiography, Proc. Soc. Photo-Opt. Instrum. Eng.* 314, 1981, pp. 72–76.

[13] Harris JL. "Resolving Power and Decision Theory." J Opt Soc Am A54:606–611, 1964.

[14] Myers KJ, Rolland JP, Barrett HH, Wagner RF. "Aperture Optimization for Emission Imaging: Effect of a Spatially Varying Backgrounds." J Opt Soc Am A7:1279–1293, 1990.

[15] Rolland JP. "Factors Influencing Lesion Detection in Medical Imaging." Ph.D Dissertation, University of Arizona, 1990.

[16] Rolland JP, Barrett HH. "Effect of Random Background Inhomogeneity on Observer Detection Performance." J Opt Soc Am A9:649–658, 1992.

[17] Burgess AE. "Statistically-Defined Backgrounds: Performance of a Modified Nonprewhitening Observer Model." J Opt Soc Am A11:1237–1242, 1994.
[18] Eckstein MP, Whiting JS. "Lesion Detection in Structured Noise." Acad Radiol 2:249–253, 1995.
[19] Judy PF. "Detection of Clusters of Simulated Calcifications in Lumpy Noise Backgrounds." Proc SPIE 2712, 1996, pp. 39–46.
[20] Whitting JS, Eckstein MP, Moriaka CA, Eigler NL. "Effect of Additive Signal Contrast and Feature Motion on Visual Detection in Structured Noise." Proc SPIE 2712, 1996, pp. 26–38.
[21] Gallas BD, Barrett HH. "Detectability for a Lumpy Background Model as a Function of Background Parameters." OSA Annual Meeting (abstract) 1997.
[22] Cargill EB. "A Mathematical Liver Model and Its Application to System Optimization and Texture Analysis." Ph.D Dissertation, University of Arizona, 1989.
[23] West BJ, Goldberger AL. "Physiology in Fractal Dimensions." American Scientist 75:354–365, 1987.
[24] Harper C. *Introduction to Mathematical Physics*. Englewood Cliffs: Prentice Hall, 1976, pp. 217–218.
[25] Park D. *Introduction to the Quantum Theory*. New York: McGraw-Hill, 1974, pp. 631–646.
[26] Rappaport AM, McPhee PJ, Fisher MM, Phillips MJ. "The Scarring of the Liver Acini (Cirrhosis)." Virchows Archive A402:107–137, 1983.
[27] Fink M, Hottier F, Cardoso JF. "Ultrasonic Signal Processing for In-Vivo Attenuation Measurement: Short Time Fourier Analysis." Ultrasonic Imaging 5:117–135, 1983.
[28] Insana MF, Wagner RF, Garra BS, Brown DG, Shawker TH. "Analysis of Ultrasonic Image Texture Via Generalized Rician Statistics." Optical Engineering 25(6):743–748, 1986.
[29] Wagner RF, Insana MF, Brown DG. "Unified Approach to the Detection and Classification of Speckle Texture in Diagnostic Ultrasound." Opt Eng 25(6):738–742, 1986.
[30] Momenan R, Wagner RF, Loew MH, Insana MF, Garra BS. "Characterization of Tissue from Ultrasound Images." IEEE Control Systems Magazine 49–53, 1988.
[31] Valckx FMJ, Thijssen JM. "Characterization of Echographic Image Texture by Cooccurence Matrix Parameters." Ultrasound in Med and Biol 23(4):559–571, 1997.
[32] Goodman JW. *Statistical Optics*. New York: John Wiley and Sons, 1985.
[33] Middleton D. *An Introduction to Statistical Communication Theory*. New York: McGraw-Hill, 1960.
[34] Fellingham-Joynt L. "A Stochastic Approach to Ultrasonic Tissue Characterization." Ph.D thesis, Stanford University, also published as Tech. Report No G 557-4, 1979.

[35] Wear KA, Wagner RF, Brown DG. "Statistical Properties of Estimates of Signal-to-Noise Ratio and Number of Scatterers per Resolution Cell." J Acoust Soc Am 102(1):635–641, 1997.
[36] Shung KK, Sigelmann RA, Reid JM. "Scattering of Ultrasound by Blood." IEEE Trans Biomed Eng BME-23:460–467, 1976.
[37] Goodman JW. "Statistical Properties of Laser Speckle Patterns." In Dainty JC (Ed.) *Laser Speckle and Related Phenomena*. Berlin: Springer-Verlag, 1975, pp. 9–75.
[38] Wagner RF, Smith SW, Sandrik JM, Lopez H. "Statistics of Speckle in Ultrasound B-Scans." IEEE Trans Sonics Ultrason SU-30:156–163, 1983.
[39] Wagner RF, Insana MF, Brown DG. "Statistical Properties of Radio-Frequency and Envelope-Detected Signals with Applications to Medical Ultrasound." J Opt Soc Am A4:910–922, 1987.
[40] Strickland RN. "Wavelet Transforms for Detecting Microcalcifications in Mammograms." IEEE Transactions on Medical Imaging 15(2):218–229, 1996.
[41] Rolland JP, Strickland R. "An Approach to the Synthesis of Biological Tissue." Optics Express 1(13) 1997.
[42] Nicholson PHF, Mueller R, Lowet G, Cheng XG, Hildebrand T, Ruegsegger P, Van der Perre G, Dequeker J, Boonen S. "Do Quantitative Ultrasound Measurements Reflect Structure Independently of Density in Human Vertebral Cancellous Bone?" Bone 23:425–431, 1998.
[43] Rolland JP, Goon A, Yu L. "Synthesis of Textured Complex Backgrounds." Opt Eng 37(7):2055–2063, 1998.
[44] Harris C. "Normalized Second-Order Statistics for Texture Characterization." Master Dissertation, University of Central Florida, Orlando FL, 1999.
[45] Heeger DJ, Bergen JR. "Pyramid-Based Texture Analysis/Synthesis." Computer Graphics Proceedings 229–238, 1995.
[46] Vaidyanathan PP. *Multivariate Systems and Filter Banks*. Englewood Cliffs, NJ: Prentice Hall, 1993.
[47] Woods JW. *Subband Image Coding*. Norwell MA: Kluwer Academic Publishers, 1991, pp. 43–192.
[48] Simoncelli EP, Freeman WT, Adelson EH, Heeger DJ. "Shiftable Multi-Scale Transforms." IEEE Transactions on Information Theory, Special Issue on Wavelets 38:587–607, 1992.
[49] Perona P. "Deformable Kernels for Early Vision." IEEE Transactions on Pattern Analysis and Machine Intelligence 7(5):488–489, 1995.
[50] Simoncelli EP, Freeman WT. "The Steerable Pyramid: A Flexible Architecture for Multi-Scale Derivative Computation." In *Proc IEEE Int Conf Image Processing*, Washington, DC, 1995.
[51] Castleman KR. *Digital Image Processing*. Upper Saddle River NJ: Prentice Hall, 1996.
[52] Hall EH. "Almost Uniform Distributions for Computer Image Enhancement." IEEE Trans Comput C-23(2):207–208, 1974.

[53] Pizer SM, Amburn EP, Austin JD, Cromartie R, Geselowitz A, Greer T, Romeny BTH, Zimmerman J, Zuiderveld K. "Adaptive Histogram Equalization and Its Variations." Computer Vision, Graphics, and Image Processing 39:355–368, 1987.
[54] Paranjape RB, Morrow WM, Rangayyan RM. "Adaptive-Neighborhood Histogram Equalization for Image Enhancement." Graphical Models and Image Processing 54(3):259–267, 1992.
[55] Rolland JP, Vo V, Abbey CK, Yu L, Bloss B. "Fast Algorithms for Histogram Matching: Application to Texture Synthesis." Journal of Electronic Imaging 9(1), 2000.
[56] Julez B. "Visual Pattern Discrimination." IRE Trans Inform Theory 8(2):84–92, 1962.
[57] Haralick RM. "Statistical and Structural Approaches to Texture." Proc IEEE 67(5):786–804, 1979.
[58] Bochud FO, Verdun FR, Hessler C, Valley JF. "Detectability on Radiological Images: The Influence of Radiological Noise." Proc SPIE 2436, 1995, pp. 156–164.
[59] Thomson MGA, Foster DH. "Role of Second- and Third-Order Statistics in the Discriminability of Natural Images." J Opt Soc Am A14(9):2081–2090, 1997.
[60] Goon A, Rolland JP. "Texture Classification Based on Comparison of Second-Order Statistics I: 2P-PDF Estimation and Distance Measure." J Opt Soc Am A16(7):1566–1574, 1999.
[61] Harris C. "Normalized Second-Order Statistics for Texture Characterization." Master Thesis, University of Central Florida, 1999.
[62] Weir KA, Wagner RF, Brown DG, Insana MF. "Statistical Properties of Estimates of Signal-to-noise Ratio and Number of Scatterers per Resolution Cell." J Acoust Soc Am 102(1):635–641, 1999.

CHAPTER 14
Quantitative Image Quality Studies and the Design of X-Ray Fluoroscopy Systems

David L. Wilson
Case Western Reserve University and University Hospitals of Cleveland

Kadri N. Jabri, Ravindra M. Manjeshwar
Case Western Reserve University

CONTENTS